Dalton Transactions

Accepted Manuscript

This article can be cited before page numbers have been issued, to do this please use: P. Oviedo, G. E. Pieslinger, A. Cadranel and L. M. Baraldo, *Dalton Trans.*, 2017, DOI: 10.1039/C7DT02422C.




ROYAL SOCIETY OF CHEMISTRY

rsc.li/dalton

View Article Online
DOI: 10.1039/C7DT02422C



# Exploring the Localized to Delocalized Transition in Non-Symmetric Bimetallic Ruthenium Polypyridines

*Paola S. Oviedo,*[a,b] *German E. Pieslinger*[a,b] *Alejandro Cadranel,*[a,b,c] *and Luis M. Baraldo*[a,b]

[a] Universidad de Buenos Aires, Facultad de Ciencias Exactas y Naturales, Departamento de Química Inorgánica, Analítica y Química Física, Pabellón 2, Ciudad Universitaria, C1428EHA, Buenos Aires, Argentina.

[b] CONICET – Universidad de Buenos Aires. Instituto de Química-Física de Materiales, Ambientes y Energía (INQUIMAE), Pabellón 2, Ciudad Universitaria, C1428EHA, Buenos Aires, Argentina.

[c] Current address: Department of Chemistry and Pharmacy & Interdisciplinary Center for Molecular Materials, Friedrich-Alexander-Universität Erlangen-Nürnberg, 91058, Erlangen, Germany.

**Abstract**

In this work, we report the evolution of the properties of the inter-valence charge transfer (IVCT) transition in a family of cyanide-bridged ruthenium polypyridines of general formula $[Ru^{II}(tpy)(bpy)(\mu\text{-}CN)Ru^{III}(bpy)_2(L)]^{3/4+}$ (tpy = 2,2',6',2''-terpyridine; bpy = 2,2'-bipyridine; L= $Cl^-$, $NCS^-$, 4-dimethylaminopyridine or acetonitrile. In these complexes, the redox potential difference between both ruthenium centers (ΔE) is systematically modified. A decrease in ΔE causes a red shift of the energy and an intensity enhancement of the observed IVCT transitions. For L = acetonitrile, the IVCT band becomes narrower and asymmetrical, and shows very little dependence on the nature of the solvent, suggesting a delocalized configuration, although a non-symmetrical one. Also, additional electronic

View Article Online
DOI: 10.1039/C7DT02422C

transitions of low energy are clearly resolved in this complex. The observed variation in the properties of the IVCT transitions can be understood on the basis of DFT calculations, that point to increasing mixing between the dπ orbitals of both Ru ions.

**Keywords**

Ruthenium Polypyridine, Cyanide Bridge, Mixed Valence Compounds, Intervalence Charge Transfer, Metal-metal Interactions, Delocalization, (TD)DFT.





## Introduction

Electron transfer can be found in chemical, physical and biological systems, and plays a key role in catalysis and energy conversion.[1–3] Mixed-valence systems very often present inter-valence charge transfer absorption bands (IVCT), whose energy and shape are related to the pathway that drives the electron from one center to the other.[4,5] Thus, IVCT bands have been studied to evaluate the impact of different variables -redox potentials, nature of the bridge, donor-acceptor distance, solvent interactions, ionic strength- on the electron transfer process.[6–8]

According to the degree of interaction between the metal ions, symmetrical mixed-valence systems have been classified in different classes by Robin and Day.[9] Class I includes those systems where the metallic centers are uncoupled. Metal ions in complexes of Class II are weakly coupled, and they present IVCT bands that are usually weak ($\varepsilon \leq 5000$ $M^{-1}cm^{-1}$) and wide ($\Delta\nu_{1/2} \geq 2000$ $cm^{-1}$). Class III systems are characterized by potential energy surfaces with only one minimum, where both metal centers have an intermediate oxidation state and hence they are described as delocalized. These systems present more intense electronic transitions that occur between molecular orbitals delocalized over the entire bimetallic fragments and, in principle, they do not involve net charge transfer between the fragments. These IVCT

View Article Online
DOI: 10.1039/C7DT02422C



bands are intense ($\varepsilon \geq 5000\ M^{-1}cm^{-1}$) with narrow bandwidths ($\Delta\nu_{1/2} \leq 2000\ cm^{-1}$) and a cut-off at the low energy side. In addition, a Class II/III has been defined by Meyer.[6] It comprises still localized systems described by potential energy surfaces with two minima, but these minima are separated by a small energy barrier, so both electronic isomers interconvert very rapidly and as a result they are solvent-averaged.[7]

The above classification can be extended to include also non-symmetrical systems where the energy of the two possible electronic isomers is not equal. In this case, a strong coupling could result in a localized system (Class II), if one configuration is heavily favored; or in a delocalized system (Class III), if the energy difference between the electronic isomers is smaller. However, in this case, the resulting minimum for the potential energy surface may not have an even charge distribution. Thus, for non-symmetrical Class III systems, the IVCT band may present some residual charge transfer character, but it still involves molecular orbitals delocalized over both fragments and should be both intense and narrow.

The lack of symmetry in mixed-valence systems can have two origins. It may arise from different chemical environments around the moieties involved in the electron transfer[10,11], or from non-symmetric bridges connecting those moieties, like in the case of the cyanide anion, which is one of the most thoroughly explored.[12–15] Most of this studies conclude that cyanide is able to promote strong electronic coupling between metal centers,[13,16–18] although very few of these complexes have been described as Class III systems.[19–22] This is due to the redox asymmetry introduced by the nature of the cyanide bridge, in which coordination by C atom stabilizes the donor site.

Previous reports show that the effect of the cyanide bridge can be mitigated when the electronic properties of the linked metallic ions are adequately tuned.[20,21] Here we report a family of non-symmetrical cyanide-bridged complexes, [$Ru^{II}$(tpy)(bpy)(μ-

View Article Online
DOI: 10.1039/C7DT02422C



CN)$Ru^{II}(bpy)_2(L)]^{2+/3+}$ (Scheme 1), where the difference in redox potential between the Ru ions (ΔE) can be systematically varied changing the nature of L. This allowed us to explore the impact of this variable on the properties of the IVCT band and to categorize these systems in the Robin and Day classification. More importantly, these systems provide us with good spectroscopic markers to assign the degree of mixing between the metallic dπ orbitals in cyanide-bridged systems. These markers will facilitate the identification of systems with extended delocalization, a topic of relevance as the different configuration can trigger a very different reactivity. An example of the latter is a trimetallic system recently reported by us,[23] where the energy transfer process between the terminal moieties was observed by photophysical and ultrafast time-resolved absorption experiments. In this system a delocalized excited state is instrumental in promoting the observed the energy transfer. The result suggests that identification of delocalization in the excited state could lead to systems able to effectively engage in energy or electron transfer processes in extended systems, making them an appealing platform for the design of chromophore-catalyst assemblies.

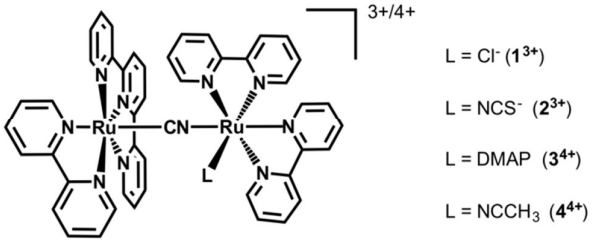


**Scheme 1.** Structure of the mixed-valence complexes studied in this work (DMAP = 4-dimethylaminopyridine).

## Experimental procedures

View Article Online
DOI: 10.1039/C7DT02422C



**Materials**. $[Ru(bpy)_2(CO_3)]_2$[24] and $[Ru(tpy)(bpy)CN](PF_6)$,[25] were prepared following literature methods. All other materials were of reagent grade, obtained from commercial sources and used without further purification. Solvents for electrochemical, spectral and spectroelectrochemical measurements were dried using a PureSolv Micro solvent purification system. Chromatographic separations were made with Sephadex LH20 eluted with methanol. All the compounds were dried in a vacuum desiccator for at least 12 hours prior to characterization.

**Physical Measurements**. Absorption spectra in the UV-vis/near-IR regions were taken with a Hewlett-Packard 8453 diode array spectrometer (range 190–1100 nm). NIR/IR spectra were recorded with a Nicolet iS10 FT-IR spectrometer (range 12000-400 $cm^{-1}$). $^1$H-NMR spectral data were acquired with a Bruker ARX500 spectrometer, using deuterated solvents from Aldrich. Elemental analyses were carried on a Carlo Erba 1108 analyzer with an estimated error of ± 0.5%. Electrochemical measurements were performed under argon with millimolar solutions of the compounds, using a TEQ V3 potentiostat and a standard three electrode arrangement consisting of a glassy carbon disc (area = 9.4 $mm^2$) as the working electrode, a platinum wire as the counter electrode and a silver wire as reference electrode plus an internal ferrocene (Fc) standard. The supporting electrolyte was Tetra-*n*-butylammonium hexafluorophosphate ($[TBA]PF_6$, 0.1 M). All the potentials reported in this work are referenced to the standard Ag/AgCl saturated KCl electrode (0.197 V vs. NHE), the conversions being performed with literature values for the $Fc^+$/Fc couple.[26] All the spectroelectrochemical (SEC) experiments were performed using a three-electrode OTTLE cell,[27] with millimolar solutions of the compounds using $[TBA]PF_6$ 0.1 M as the supporting electrolyte.

View Article Online
DOI: 10.1039/C7DT02422C



**X-ray Structure Determination.** Crystal structure of compound **1** was determined with an Oxford Xcalibur, Eos, Gemini CCD area-detector diffractometer using graphite-monochromated Mo-*K*α radiation ($\lambda$ = 0.7107 Å) at 298 K. Data was corrected for absorption with CrysAlisPro, Oxford Diffraction Ltd., Version 1.171.33.66, applying an empirical absorption correction using spherical harmonics, implemented in SCALE3 ABSPACK scaling algorithm.[28] The structure was solved by direct methods with SIR97[29] and refined by full-matrix least-squares on $F^2$ with SHELXL-2014[30] under WinGX platform[31]. Hydrogen atoms were added geometrically and refined as riding atoms with a uniform value of $U_{iso}$. Some fluorine atoms in the three counterions were found disordered around two positions and split refined with fixed 0.5:0.5 occupancy factors. Disordered lattice solvent molecules that could not be refined satisfactorily were handled by using the SQUEEZE option in PLATON[32]. Final crystallographic data and values of $R_1$ and *wR* are listed in Table S1 while the main angles and distances are listed in Table S2. CCDC 1538264 contains the supplementary crystallographic data for this paper. These data can be obtained free of charge from the Cambridge Crystallographic Data Center via www.ccdc.cam.ac.uk/data_request/cif.

**Synthetic Procedures**

**$[Ru^{II}(tpy)(bpy)(\mu\text{-}CN)Ru^{II}(bpy)_2(L)](PF_6)_{2/3}$ (L = OH/$OH_2$). (*solid A*)** To a solution of [Ru(tpy)(bpy)(CN)]($PF_6$) (150mg, 0.23 mmol) in deoxygenated acetone (150 mL), 125mg (0.39 mmol) of Ru(bpy)($CO_3$) were added together with three drops of trifluoroacetic acid. The mixture was heated at reflux for 2 hours under Ar atmosphere and 1.2 eq. of $KPF_6$ (86 mg) were added to the hot solution together with 15ml $H_2O$(d). The brown solution was concentrated on a rotary evaporator until only water remained. After cooling at room temperature, a brown solid was collected by filtration, washed with water, and dried. 225mg of ***solid A*** were obtained.

View Article Online
DOI: 10.1039/C7DT02422C



**[Ru(tpy)(bpy)(μ-CN)Ru(bpy)$_2$(Cl)](Cl)$_2$ (1)** 50mg of ***solid A*** together with 3 mL of HCl(c) were heated at reflux in 30ml for 2 hours. After the mixture cooled down to room tempreature, the solvents were evaporated until dryness. The resulting solid was loaded in a Sephadex LH20 column (l = 30 cm and ϕ = 4 cm) and eluted with methanol. The solvent of the second brown-red fraction collected was removed under vacuum until dryness and recrystallized from acetone: water (1:1). Yield 32mg, 72.5%. Anal. calcd. for **1·8H$_2$O**: C, 46.8; H, 4.4; N, 11.9. Found: C, 47.0; H, 4.0; N, 11.7. $^1$H NMR (500 MHz, solvent DMSO d$_6$, Figure S1) δ 9.64 (dd, 1H), 9.23 (dd, 1H), 8.87 (dd, 1H), 8.73 (m, 2H), 8.68 (d, 1H), 8.63 (m, 3H), 8.57 (d, 1H), 8.50 (d, 1H), 8.46 (d, 1H), 8.31 (m, 3H), 8.08 (m, 3H), 8.01 (m, 1H), 7.93 (m, 1H), 7.83 (m, 1H), 7.77 (ddd, 1H), 7.71 (m, 2H), 7.52 (m, 3H), 7.39 (ddd, 1H), 7.28 (m, 2H), 7.22 (m, 2H), 7.14 (ddd, 1H), 7.08 (m, 1H), 6.97 (ddd, 1H).

**[Ru(tpy)(bpy)(μ-CN)Ru(bpy)$_2$(SCN)](PF$_6$)$_2$ (2)** To a partial solution of ***solid A*** (50 mg) in acetone (15 mL) a solution of KSCN (35 mg, 0.36 mmol) in water (15 mL) was added. The mixture was heated at reflux for 7 days. The solution was concentrated on a rotary evaporator until only water remained. The product was collected on a frit, washed with water, and dried. Purification was achieved by recrystallization from acetone:water (1:1) together with 1.2 eq of KPF$_6$ to obtain hexafluorophosphate salts. Yield: 30mg, 67.5%. Anal. calcd. for **2·2H$_2$O·3MeOH**: C, 42.6; H, 3.6; N, 10.9; S, 2.3. Found: C, 42.8; H, 3.3; N, 10.6; S, 3.0. $^1$H NMR (500 MHz, solvent acetone d$_6$, Figure S1) δ 9.79 (d, 1H), 9.30 (d, 1H), 8.90 (d, 1H), 8.84 (d, 1H), 8.65 (m, 3H), 8.62 (m, 2H), 8.52 (d, 1H), 8.49 (d, 1H), 8.43 (d, 1H), 8.33 (m, 3H), 8.14 (m, 3H), 8.08 (m, 2H), 8.03 (s, 8H), 7.99 (dd, 1H), 7.99 (m, 3H), 7.81 (m, 2H), 7.63 (d, 1H), 7.52 (m, 3H), 7.37 (m, 2H), 7.25 (dd, 2H), 7.09 (dd, 1H).

View Article Online
DOI: 10.1039/C7DT02422C



**[Ru(tpy)(bpy)(μ-CN)Ru(bpy)$_2$(DMAP)](PF$_6$)$_3$ (3)** 50mg of ***solid A*** together with 25mg of DMAP in 30ml acetone were heated at reflux for one day. After the mixture cooled down to room temperature, the solvent was removed under vacuum. The resulting solid was dissolved in a minimum volume of methanol and loaded on a Sephadex LH-20 column (l = 30 cm, ⌀ = 4 cm) packed and eluted with methanol. The second brown-red fraction collected was evaporated until dryness and recrystallized from acetone:water (1:1). Yield 35mg, 67.5%. Anal. calcd. for **3·2MeOH**: C, 42.6; H, 3.5; N, 10.8. Found: C, 42.9; H, 3.3; N, 10.6. $^1$H NMR (500 MHz, solvent acetone d$_6$, Figure S1) δ 9.65 (d, 1H), 9.08 (d, 1H), 8.94 (ddd, 2H), 8.87 (d, 1H), 8.80 (m, 4H), 8.75 (d, 1H), 8.69 (t, 2H), 8.65 (t, 2H), 8.38 (ddd, 1H), 8.33 (ddd, 1H), 8.28 (d, 1H), 8.24 (ddd, 1H), 8.11 (m, 4H), 8.03 (ddd, 1H), 7.95 (m, 5H), 7.79 (d, 1H), 7.73 (m, 3H), 7.65 (m, 2H), 7.58 (ddd, 2H), 7.50 (d, 1H), 7.43 (ddd, 1H), 7.39 (m, 2H), 7.33 (ddd, 1H), 7.24 (ddd, 1H), 7.16 (ddd, 1H), 6.45 (dd, 2H).

**[Ru(tpy)(bpy)(μ-CN)Ru(bpy)$_2$(CH$_3$CN)](PF$_6$)$_3$ (4)** A solution of the ***solid A*** (50 mg) in acetonitrile (50 mL) was refluxed for 2 hours, and then the solvent was evaporated to dryness on a rotary evaporator. Purification was achieved by recrystallization from acetonitrile:water (1:1). Yield 45mg, 90.0%. Anal. calcd. for **4·2H$_2$O**: C, 40.0; H, 2.9; N, 10.7. Found: C, 40.1; H, 2.7; N, 10.3. $^1$H NMR (500 MHz, solvent acetone d$_6$, Figure S1) δ 9.38 (ddd, 1H), 9.07 (ddd, 1H), 8.75 (ddd, 1H), 8.57 (ddd, 1H), 8.43 (ddd, 1H), 8.36 (m, 2H), 8.34 (m, 1H), 8.29 (m, 3H), 8.23 (m, 1H), 8.21 (m, 1H), 8.19 (m, 1H), 8.15 (m, 1H), 8.12 (m, 1H), 8.05 (m, 1H), 7.97 (m, 2H), 7.85 (m, 3H), 7.78 (m, 1H), 7.64 (m, 2H), 7.57 (m, 2H), 7.41 (m, 1H), 7.40 (m, 1H), 7.21 (m, 2H), 7.16 (m, 2H), 7.11 (m, 1H), 7.03 (m, 1H).

**Theoretical calculations**

View Article Online
DOI: 10.1039/C7DT02422C



Density Functional Theory (DFT) computations were employed to fully optimize the geometries of the complexes in acetonitrile, without symmetry constraints. The geometries of the singlet ground state were optimized and serve as the starting point for the optimization of the oxidized species. The calculations were done with the *Gaussian09* package,[33] at the B3LYP level of theory using restricted and unrestricted approximations of the Kohn-Sham equations, depending on the total number of electrons.[34] In all cases, we employed the effective core potential basis set LanL2DZ, which proved to be suitable for geometry predictions in coordination compounds containing metals of the second row of the transition elements in the Periodic Table. All the calculations were performed using an UltraFine grid. Solvation effects were accounted for using the most recent implementation of the implicit IEF-PCM solvation model.[35–37] We used tight convergence criteria in the geometry optimizations and default settings for IR calculations. All optimized structures were confirmed as minima by analyzing the harmonic vibrational frequencies.[38] Vertical electronic excitation energies and intensities were evaluated using time-dependent DFT ((TD)DFT)[39,40] approach with the *Gaussian09* package,[33] without symmetry constraints. GaussSum 2.2.6[41] software was used to perform spectral simulation, to extract spectral data and molecular orbital information and to obtain the electron density difference maps (EDDM). The graphical visualizations were generated by GaussView5.0.8,[42] i.e., the isovalues were drawn at 0.004 (EDDM), 0.04 (Kohn−Sham MOs), or 0.004 (spin-density calculations). The EDDM, the composition of electronic transitions, and the associated molecular orbitals for all the calculated complexes are shown in the Electronic Supporting Information.

## Results

View Article Online
DOI: 10.1039/C7DT02422C



**X-ray Structure Determinations**. The crystallographic structure of complex [**4**]$(PF_6)_3$ is shown in Figure 2. Selected bond distances and angles are summarized in Table S2. This molecule presents the usual characteristics of {Ru(tpy)} and {Ru$(bpy)_2$} moieties.[25,43] The central ring of the tpy ligand shows a short Ru–N distance, and the bite angles of the {Ru(tpy)} fragment deviate from the 90° expected for an octahedral environment. These are a result of the rigid planar structure of this tridentate ligand, that constrains geometry around the metal ion. In the {Ru$(bpy)_2$} moiety, $Ru_{b2}$–N bonds and angles are in the range expected for Ru(II) polypyridines. The {Ru-Ru} structure is less linear than in related complexes,[25,44] presenting a significant torsion angle of 36° around the cyanide bridge. This is a consequence of π-π stacking interactions (Figure S1) in the crystal. These are not expected to play a role in solution, where the torsion angle is likely to be considerably smaller.

Importantly, DFT geometry optimizations reproduce well the structural characteristics observed experimentally (Table S2), although they predict an almost linear {Ru-Ru} moiety. This discrepancy was expected since the theoretical method employed does not take into account the packaging effects observed in the crystal. It is worth to mention here that DFT geometry optimizations were performed to study the complexes properties in solution, and the electronic transitions predicted for all the species are in good agreement with the experimental results.

View Article Online
DOI: 10.1039/C7DT02422C



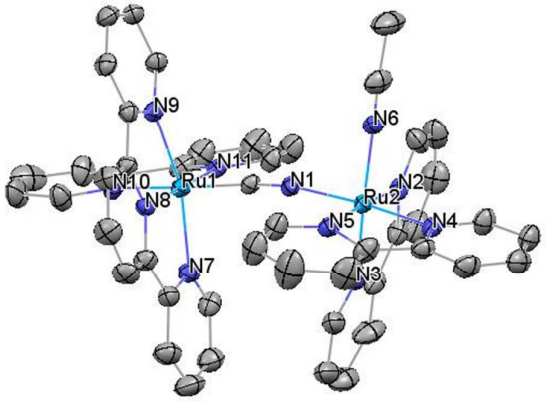


**Figure 1.** Structural representation of the complex [**4**]$(PF_6)_3$ with hydrogen atoms omitted for the sake of clarity. The thermal ellipsoids correspond to 20% probability.

## Electrochemistry

Cyclic and square wave voltammograms for complexes $\mathbf{1}^{2+}$- $\mathbf{4}^{3+}$ in acetonitrile are shown in Figure 2. All these compounds present two one-electron reversible or quasi-reversible waves in the anodic region that can be assigned to Ru-centered oxidation processes, except for $\mathbf{2}^{2+}$ that shows a different behavior (Figures 1 and S3) that will be discussed at the end of this section. The asymmetry of the cyanide bridge guides the assignment of the signals observed. The C terminus of the bridge presents a pronounced acceptor character, which in synergy with the electron acceptor polypyridines, results in potentials over 1.5 V for the {Ru(tpy)(bpy)(μ-CN)} moiety, close to that observed for the same fragment in related complexes.[23,45] In these molecules, the oxidation process of the {Ru(tpy)(bpy)} fragment is shifted to higher potentials in comparison to the monometallic $[Ru(tpy)(bpy)(CN)]^{+}$,[25] due to the presence of a cyanide-bridged Ru(III) in the bimetallic compounds. Electrochemical waves at lower potentials are assigned to the metal ion in $\{Ru(bpy)_2(L)(\mu\text{-}NC)\}$. This is due to the weaker electron accepting N terminus of the bridge, and to the L ligand occupying the sixth coordination position. L varies from the strongly donating chloride

View Article Online
DOI: 10.1039/C7DT02422C



(in $\mathbf{1}^{2+}$) to acetonitrile (in $\mathbf{4}^{3+}$), that behaves as an acceptor in Ru(II) complexes.[46,47] This is reflected in the increase of the redox potential of the {Ru(bpy)$_2$} moiety when moving from $\mathbf{1}^{2+}$ to $\mathbf{4}^{3+}$ (Figure 2 and Table 1), although the observed increase is smaller than that one observed in Ru(II) mononuclear complexes.[46–49] Accordingly, the ΔE between the ruthenium ions diminishes in the same order, even though it is still large for $\mathbf{4}^{3+}$.

In the case of $\mathbf{2}^{2+}$, four signals are observed at 0,94 V, 1.30 V, 1.57 V and 1.77 V. We ascribe the wave at 0.94 V to the oxidation of the Ru ion in the {Ru(bpy)$_2$} fragment, following the arguments exposed before, i.e. the asymmetry of the cyanide bridge and comparisons with related monomers. The assignment of the signals at 1.30V, 1.57 and 1.77 V require a more detailed analysis. The latter perfectly matches that one recorded for the second oxidation process of $\mathbf{4}^{3+}$, indicating the formation of the acetonitrile complex during the electrochemical experiment. Additionally, when the scan is reversed, a reduction half-wave at 1.30 V appears, that correspond to the first oxidation process of $\mathbf{4}^{3+}$. The corresponding oxidation half-wave is absent in the first oxidative scan. Consistently, when SW voltammetry is carried out in anodic scan directions, only three waves are observed. Notably, this oxidation half-wave is observed if further cycles are performed (Figure S3). Nevertheless, no signal appears at 1.30 V upon cycling if the scans reach a maximum potential of 1.5 V (Figure S3, inset). Hence, we assign the process at 1.57 V as the oxidation of $\mathbf{2}^{2+}$. An unequivocal assignment of this signal, i.e. whether it is mainly metal- or NCS-centered, remains elusive. It has been shown that oxidation of mononuclear ruthenium(II)-thiocyanate complexes involves orbitals that spread over the entire {Ru$^{II}$(NCS)} fragment,[50] which can lead to substitution of the NCS$^-$ ligand in a timescale much shorter than that of the electrochemical experiment.[51,52] Either way, the second oxidation process of $\mathbf{2}^{2+}$ triggers

View Article Online
DOI: 10.1039/C7DT02422C



to the formation of the acetonitrile complex in its mixed-valence form. As the CV experiments show upon repetitive cycles, the conversion is fast but not complete. UV-vis and NIR/IR spectroelectrochemical studies (*vide infra*) are consistent with this assignment.

| | | $E_{1/2}$ ($E_a$-$E_c$)/ V (mV) | | |
|---|---|---|---|---|
| complex | L | $Ru_{b2}^{III/II}$ | $Ru_{tb}^{III/II}$ | ΔE/V |
| **1** | **Cl** | 0.82 (65) | 1.63 (85) | 0.83 |
| **2** | **$SCN^-$** | 0.94 (90) | 1.57* | nd |
| **3** | **DMAP** | 1.04 (140) | 1.61 (170) | 0.58 |
| **4** | **$CH_3CN$** | 1.27 (120) | 1.73 (150) | 0.53 |

**Table 1.** Reduction potentials of the complexes **1**-**4** in acetonitrile/0.1 M [TBA]$PF_6$ vs. Ag/AgCl at 100 $mV \cdot s^{-1}$ scan rate. *An unequivocal assignment of the origin of this signal remains elusive. See text. nd: non determined.

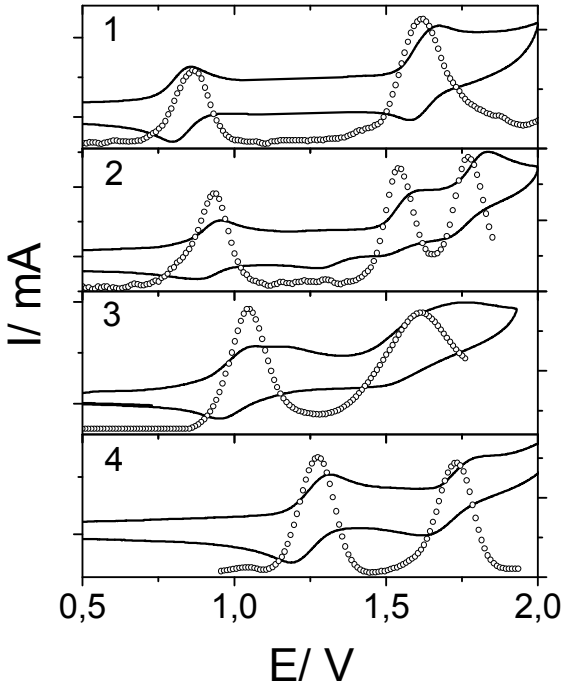


**Figure 2.** Cyclic voltammograms (solid line) and square wave voltammograms (voided circles) of **1**, **2**, **3**, and **4** in acetonitrile/0.1 M [TBA]$PF_6$ at 100 $mV \cdot s^{-1}$ scan rate vs. Ag/AgCl. See the experimental section for more details.

View Article Online
DOI: 10.1039/C7DT02422C



**VIS-NIR Spectroscopy.** The visible absorption spectra of the [II,II] species (black line, Figure 3) present intense signals in the region 22-19×$10^3$ $cm^{-1}$. We assign them to overlapping MLCT bands, that involve multiple transitions from the d$\pi$(Ru(II)) orbitals of both ruthenium centers to the low-lying $\pi^*$ orbitals of the polypyridinic ligands. The presence of two overlapping bands is more evident in the spectrum of $\mathbf{1}^{2+}$, while they cannot be distinguished in the spectrum of $\mathbf{4}^{3+}$. This behavior is a consequence of the blue shift of the MLCT bands associated with the {Ru(bpy)$_2$} fragment as the L ligand becomes a worse donor and a better acceptor.[46] This effect of L is less pronounced in the transitions associated with the {Ru(tpy)(bpy)} fragment and their energy remain almost invariant. This different behavior results in the significant overlap of both bands observed for $\mathbf{4}^{3+}$.

View Article Online
DOI: 10.1039/C7DT02422C



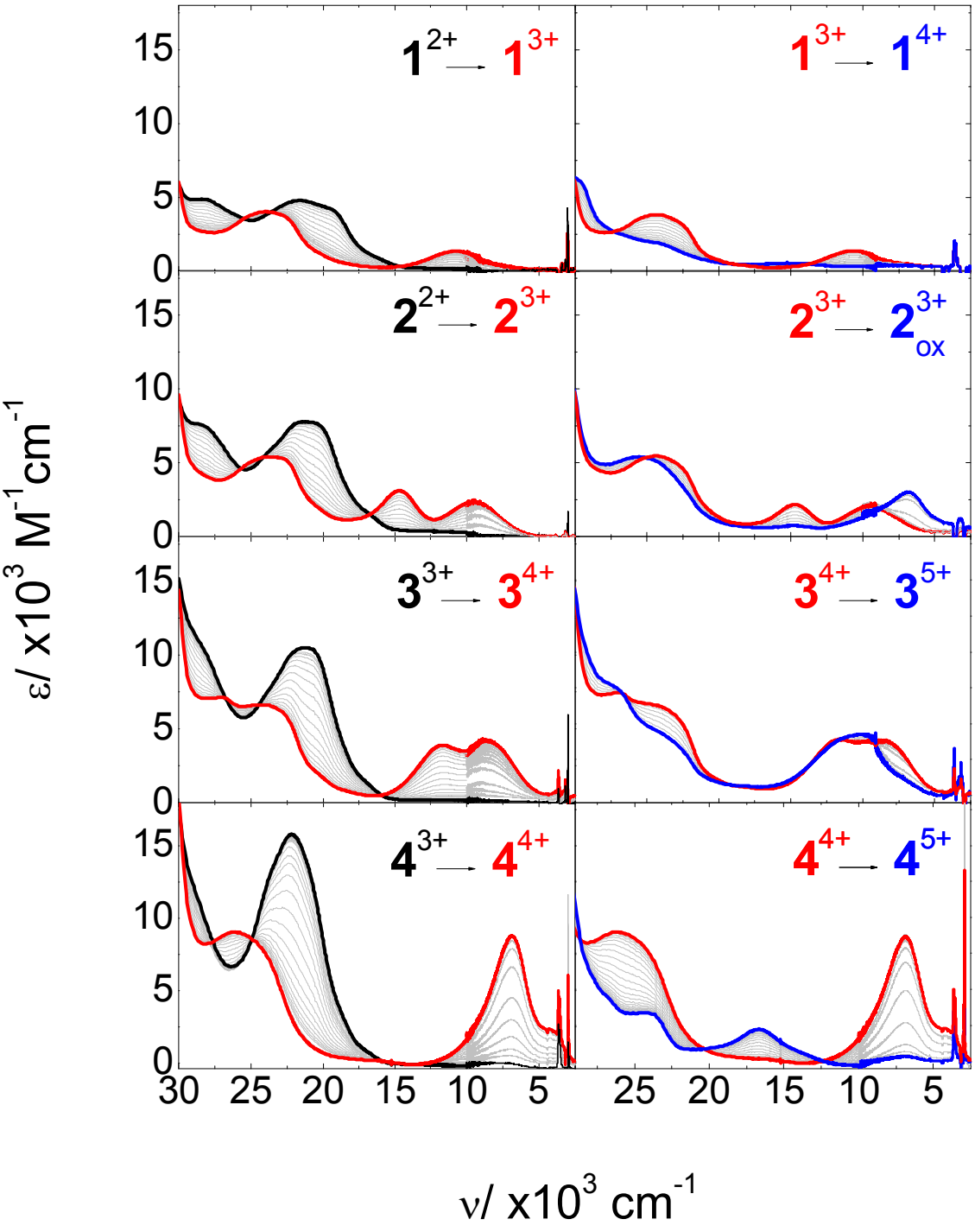


**Figure 3.** VIS−NIR spectroelectrochemistry of $\mathbf{1}^{2+}$ (top) to $\mathbf{4}^{3+}$ (bottom) in acetonitrile/0.1 M [TBA]$PF_6$, during the first (left) and second (right) oxidation processes. The spectra of the [II,II] (black), [II,III] (red), and [III,III] (blue) species are highlighted. See the experimental section for more details.

View Article Online
DOI: 10.1039/C7DT02422C



Upon one-electron oxidation of the bimetallic compounds, the MLCT bands evolve to higher energies (red lines, Figure 3). This is due to depletion of those transitions associated with the {Ru(bpy)$_2$} fragment, and a blue shift of the {Ru(tpy)(bpy)} MLCT profile arising from the presence of the Ru(III) moiety attached to the cyanide bridge. The energy and profile of this band in all the complexes is very similar, except for **4**$^{3+}$ where the blue shift is more pronounced (Figure 3 and Table 2).

Additionally, mixed-valence [II,III] species show new bands in the NIR region (red lines, Figure 3). Those that disappear upon further oxidation (blue line, Figure 3) can be assigned as IVCT transitions. For **1**$^{3+}$, the IVCT band is centered at 11800 cm$^{-1}$, and as the donor character of the L ligand decreases, it shifts to lower energies while its intensity increases (Table 2). In **4**$^{4+}$, this band is centered at 6900 cm$^{-1}$ and it is very intense ($\varepsilon$ = 9300 M$^{-1}$ cm$^{-1}$) and asymmetrical, with the half-bandwidth on the low-energy side narrower than on the high-energy side. Also, a less intense band at 4200 cm$^{-1}$ can be distinguished. The energy and the shape of these NIR bands show very little dependence on the solvent (see Figure S4)).

For the mixed-valence complexes, **2**$^{3+}$ and **3**$^{4+}$ additional features appear at 14670 and 11600 cm$^{-1}$, respectively. We assign them as LMCT transitions involving the {Ru$^{III}$(bpy)$_2$} ion and the L ligand (NCS$^-$ in **2**$^{3+}$ and DMAP in **3**$^{4+}$). As expected for a charge transfer, the energy of these transitions is solvent dependent (figure S4 and table S3).[53–56] Similar signals have been observed for related systems.[19,21,57–60] The presence of these transitions confirms our assignment of the first oxidations as {Ru(bpy)$_2$}-centered.

| | $\nu_{max}/10^3$ cm$^{-1}$ ($\varepsilon_{max}/10^3$ M$^{-1}$ cm$^{-1}$) [$\Delta\nu_{1/2}/10^3$ cm$^{-1}$] | | |
|---|---|---|---|
| **complex** | **MLCT dπ(Ru)→π*(pp)** | **LMCT π(L)→dπ(Ru)** | **IVCT** |
| **1**$^{2+}$ | 21.6-19.3 (5.0-4.1) | --- | --- |

View Article Online
DOI: 10.1039/C7DT02422C



| | | | |
|---|---|---|---|
| $\mathbf{1}^{3+}$ | 23.8 (3.8) | | 10.8 (2.6)[4.7] |
| $\mathbf{2}^{2+}$ | 21.0 (7.8) | --- | --- |
| $\mathbf{2}^{3+}$ | 23.5 (5.5) | 14.7 (3.1) | 9.5 (3.2)[4.5] |
| $\mathbf{3}^{3+}$ | 22.1 (11.3) | --- | --- |
| $\mathbf{3}^{4+}$ | 23.7 (6.7) | 11.7 (3.9) | 8.4 (4.0)[4.0]<br>3.8 (0.7)[1.5]<br>2.2 (0.5)[0.8] |
| $\mathbf{4}^{3+}$ | 22.1 (16.1) | --- | --- |
| $\mathbf{4}^{4+}$ | 25.7 (9.1) | | 6.9 (9.3)[2.9]<br>4.2 (2.3)[1.7]<br>1.6 (0.4)[1.0] |

**Table 2.** Experimental Vis-NIR data in Acetonitrile/0.1 M $[TBA]PF_6$ for complexes **1** to **4** in their different oxidation states. Only bands that are resolved in experimental spectra are included here. pp = tpy or bpy and L = $CH_3CN$, DMAP, $NCS^-$ or $Cl^-$.

The [III,III] species (blue lines, Figure 3) are characterized by the disappearance of the MLCT transitions. They are replaced by a series of weak ligand-to-metal charge transfer (LMCT) transitions involving $\pi$ orbitals of the ligands and the semi-occupied d$\pi$ orbitals of the Ru(III) centers. The exception is the complex $\mathbf{2}_{ox}^{3+}$, where the MLCT is still clearly visible, although slightly shifted to the blue. Also, this spectrum is lacking the LMCT that we assigned to the transition from the thiocyanate ligand to the Ru(III). All this evidence suggests that for the complex $\mathbf{2}^{2+}$ the second oxidation process (at 1.57 V) renders the acetonitrile complex in its mixed-valence form. In agreement with our assignment, its absorption profile is remarkably similar to that obtained upon oxidation of $\mathbf{4}^{3+}$ (see Figure S5) and very different from what is expected for the spectrum of a [III,III] like $\mathbf{2}_{ox}^{3+}$.

**IR Spectroscopy.** Spectroelectrochemical experiments in acetonitrile allowed us to characterize the vibrational spectroscopy of all complexes in the different redox states (Figures 4 and S6 and Table S4). The spectra of their [II,II] species (black lines, Figure

View Article Online
DOI: 10.1039/C7DT02422C



4) exhibit a band between 2110 and 2100 $cm^{-1}$, which can be assigned as a cyanide stretch ν(CN).[61–65] This signal is shifted to higher energies compared with that of the terminal cyanide in the related monomer $[Ru(tpy)(bpy)(CN)]^{+}$.[25] This is due to the restriction on the movement of the cyanide bridge imposed by the second ruthenium ion.[20,64–69] Compound $\mathbf{2}^{2+}$ presents an extra signal at 2105 $cm^{-1}$ that we ascribe to the stretching of the $NCS^{-}$ ligand by comparison with the spectrum of the related monomer.[25]

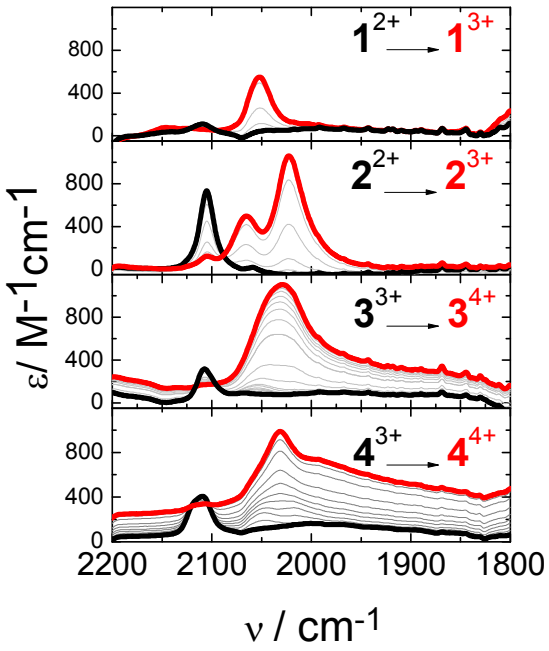


**Figure 4.** IR spectroelectrochemistry of $\mathbf{1}^{2+}$ (top) to $\mathbf{4}^{3+}$ (bottom) in acetonitrile/0.1 M $[TBA]PF_6$, during the first oxidation process. The spectra of the [II,II] (black) and [II,III] (red) species are highlighted. See the experimental section for more details.

In the one-electron oxidized forms [II,III] of the four compounds, the cyanide stretch is shifted to lower energies (red lines, Figure 5) with respect to those observed for the [II,II] species, and their intensity is greatly enhanced. This behavior was

View Article Online
DOI: 10.1039/C7DT02422C



observed in other cyanide-bridged {Ru-Ru} compounds,[20,66,69–77] and it has been assigned to vibronic coupling.[75] Specie $\mathbf{2}^{3+}$ shows an extra band around 2020 $cm^{-1}$ also enhanced by vibronic coupling that we assign as the $\nu$(SCN)[50]. Also, complexes $\mathbf{3}^{4+}$ and $\mathbf{4}^{4+}$, present two broad bands centered around 4000 $cm^{-1}$ and 2000 $cm^{-1}$ in the IR region which have electronic character (Figure S8) (*vide infra*).

For all the bimetallic complexes reported here, upon further oxidation these intense bands disappear and are replaced by a wide signal of low intensity around 2100 $cm^{-1}$ (blue line, figure S4). When L = $NCS^-$, the spectrum of the second-electron oxidation product is very similar to that of $\mathbf{4}^{4+}$ (see Figure S7), which confirms our assignment of the second oxidation process of complex $\mathbf{2}^{3+}$.

**(TD)DFT calculations.** To gain further insight into the electronic configuration of these complexes we performed DFT and (TD)DTF calculations. It is known that DFT methods can predict very accurately the properties of Class III systems,[21,78–80] but they often overestimate charge delocalization in Class II mixed-valence complexes.[79,81,82]

Figure 5 shows the spin density distribution for the four mixed-valence complexes. For complexes $\mathbf{1}^{3+}$ and $\mathbf{2}^{3+}$, the DFT calculations predict the hole located almost entirely in the $Ru_{b2}$ moiety. For compound $\mathbf{3}^{4+}$, the unpaired electron is distributed over the {$Ru_{tb}$−CN−$Ru_{b2}$} fragment with larger participation of $Ru_{b2}$ (17% $Ru_{tb}$, 74% $Ru_{b2}$). For compound $\mathbf{4}^{4+}$ the computed electron density is extended more evenly between the two metal centers (35% for $Ru_{tb}$, 59% $Ru_{b2}$).

View Article Online
DOI: 10.1039/C7DT02422C



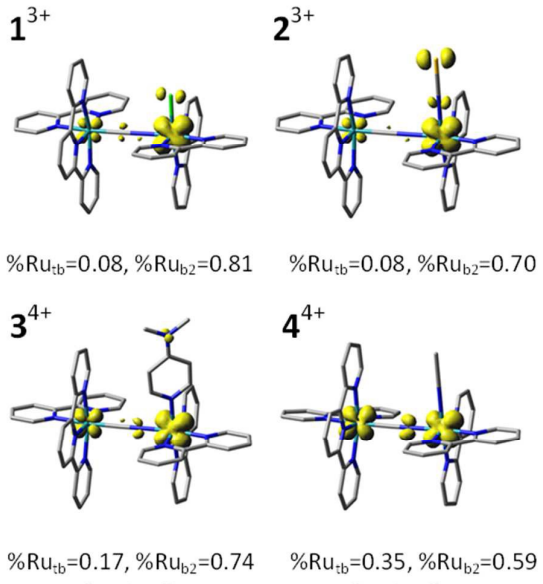


**Figure 5.** Computed spin density and Mulliken spin densities for $\mathbf{1}^{3+}$-$\mathbf{4}^{4+}$ mixed valent species.

Grey bars in Figure 6 show the electronic transitions predicted by (TD)DFT calculations for the mixed-valence species of the complexes reported here, which are in good agreement with the experimental results.

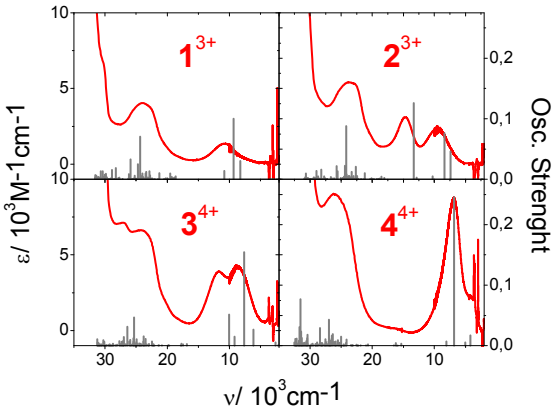


**Figure 6.** Comparison of the experimental vis-NIR spectra of the one electron-oxidized species, $\mathbf{1}^{3+}$ (left, top), $\mathbf{2}^{3+}$ (right, top), $\mathbf{3}^{4+}$ (left, bottom), $\mathbf{4}^{4+}$ (right, bottom) in acetonitrile/0.1 M [TBA]$PF_6$ and the energy of the transitions predicted by (TD)DFT calculations (bars).

View Article Online
DOI: 10.1039/C7DT02422C



The calculated visible spectrum is dominated by MLCT and LMCT transitions, while the NIR/IR region presents five calculated transitions of appreciable intensity (Tables S5, S6, S7, S8), three of them very close in energy and two others less intense at lower energy. The orbitals involved in these transitions are shown in figures S13, S15, S17 and S19. To explain the nature of these bands (see discussion), we also consider appropriate to show the "Electronic Density Difference Map" (EDDM) in figures S14, S16, S18 and S20. The EDDM is a surface that shows where electron density is gained (light blue surface) or lost (violet surface) for each transition.

Figure 7 and Table S4 show in the IR region the vibrational frequencies calculated by DFT for all the complexes in their [II,III] oxidation state (grey bars). These results are again in good agreement with experimental spectra (red lines). All mixed-valence species present one cyanide stretching around 2100 $cm^{-1}$ and compound $\mathbf{2}^{3+}$ presents one extra band predicted at 2022 $cm^{-1}$ that corresponds to the $NCS^-$ stretch.

The spin density (SD) for the [III,III] species were also calculated and the results are shown in Figure S21. All the oxidized complexes present a [III,III] configuration, although in the case of $\mathbf{2}^{3+}$ a significant part of the charge is located on the S atom of the $NCS^-$ ligand (Figure S21).

View Article Online
DOI: 10.1039/C7DT02422C



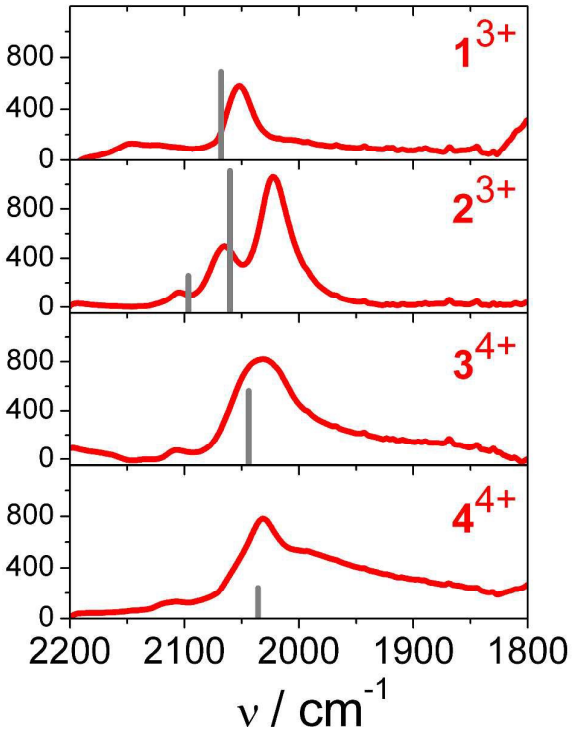


**Figure 7.** Comparison of the IR spectra of the one electron-oxidized species $\mathbf{1}^{3+}$-$\mathbf{4}^{4+}$ (from top to bottom) in acetonitrile/0.1 M [TBA]$PF_6$ and the energy of the vibrations predicted by (TD)DFT calculations (bars).

## Discussion

The modification of the L ligand in the complexes $[Ru^{II}(tpy)(bpy)(\mu\text{-}CN)Ru^{II}(bpy)_2(L)]^{3/4+}$ allows us to modify the redox potential of the $\{Ru(bpy)_2\}$ fragment. The decrease in the observed ΔE between both ruthenium centers is due to the electron donating abilities decrease (and electron acceptor character enhancement) when going from $Cl^-$ to acetonitrile. Based on the ligand parameters developed by Lever for Ru(II) complexes,[46] an increase of 0.58 V was expected when replacing $Cl^-$ by acetonitrile. However, a variation of only 0.45 V is observed for the first oxidation process. This results in a larger ΔE than expected, and in an increased stability of the mixed-valence redox state of this complex.

View Article Online
DOI: 10.1039/C7DT02422C



As the redox potential of the {Ru(bpy)$_2$} center increases, the energy of the IVCT diminishes and its intensity grows. This behavior indicates an increasing mixing between the dπ orbitals of both Ru fragments. All the IVCT transitions show very little solvent dependence. This points to very little charge transfer character in these transitions, which is also consistent with significant mixing between the orbitals involved.

The NIR spectrum observed for **4**$^{4+}$ is very distinctive (Figure 9), with a very intense and narrow band at 6900 cm$^{-1}$, that is clearly asymmetric, with a cut off at lower energies. These are the expected properties for a non-symmetric Class III mixed valence complex.[83]

For weakly coupled bimetallic dπ$^6$-dπ$^5$ compounds, three IVCT and two intraconfigurational transitions (IC) are expected due to excitation from each of the three dπ($t_{2g}$) donor orbitals on the M(II) moiety to the hole on the M(III) fragment (Figure 8). In systems with small spin-orbit coupling, the split among the dπ orbitals is small and the three IVCT transitions become overlapping bands that cannot be experimentally resolved. Furthermore, the intensity of the IC transitions is too small to be observed. Hence only one band is experimentally observed.

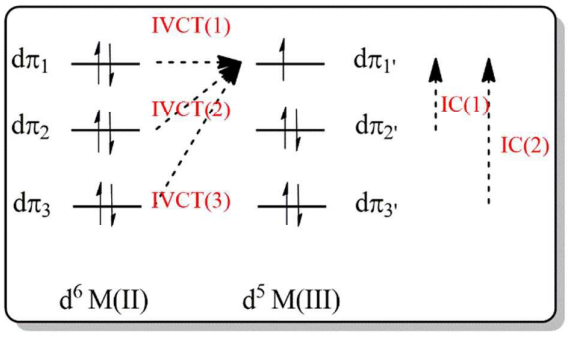


**Figure 8.** Five-band pattern for dπ$^6$-dπ$^5$ systems. In this model, only IVCT(1) arises from 'pure' electron transfer. The others are of mixed IT–IC character.

View Article Online
DOI: 10.1039/C7DT02422C



When the spin-orbit coupling is sufficiently large, it can split the $t_{2g}$ orbitals in a linear combination of atomic $d_{xy}$, $d_{yz}$, $d_{xz}$ orbitals (Kramer doublets)[6] and this leads to IVCT transitions of different energies. If these transitions have a reduced width, they can be experimentally resolved.[7] Also under this effect, the IC transitions can gain charge transfer character and became observable in the IR region.

This predicted spectral pattern of five low-energy bands has been observed in the near-IR/IR regions for complexes where the spin-orbit coupling is sufficiently large, like in mixed-valence Os dimers.[6,84,85] In this case, the high spin–orbit coupling constant ($\xi \approx 3000$ cm$^{-1}$ for Os$^{III}$) results in a split of the $d\pi^5$ Os(III) into three Kramer´s doublets, separated by thousands of cm$^{-1}$. This split shifts the IC transitions to the blue and they can be easily detected as their intensity is proportional $\xi^2$.[6] Also, the split increases the energy differences between the three IVCT transitions making the five bands pattern visible, even in the absence of significant mixing between the dπ orbitals. However, when the latter is present, it results in narrow absorption bands ($\Delta\nu_{1/2} \leq 2000$ cm$^{-1}$ for the IVCT transitions together with increased intensities and shifted energy to the blue for the IC transitions.[6,7,18,84–87] When the magnitude of the spin-orbit coupling is smaller ($\xi \approx 1000$ cm$^{-1}$ for Ru$^{III}$ and $\xi \approx 400$ cm$^{-1}$ for Fe$^{III}$), overlapping absorptions IVCT bands are usually observed. In addition, IC bands are shifted into the IR region and present greatly reduced absorptivities. However, a strong mixing of the dπ orbitals promoted by the bridge can also split the IVCT bands and boost the intensity of the IC transitions as the gain some charge transfer character. Consequently, the observation of multiple IVCT/IC bands has been informed for a very few mixed-valence Ru complexes,[20,88,89] and its observation is a clear sign of substantial mixing among the dπ orbitals.

The IR spectra of these complexes (Figure 4) also give some insight into their electronic structure. The mixed-valence complexes $\mathbf{1}^{3+}$ and $\mathbf{2}^{3+}$ show a ν(CN) band that

View Article Online
DOI: 10.1039/C7DT02422C



is more intense and shifted to lower energies with respect to those observed for the [II,II] species. This intensification is probably due to the vibronic coupling between the stretching of the cyanide bridge and the electronic transition, as proposed for other cyanide mixed-valence systems.[20,21,69,90,91] On the other hand, the electronic coupling between two metal sites involves an electron transfer mediated by the cyanide bridge, through the overlap of its π* orbitals with the dπ orbitals of the metal centers. Therefore, in [II,III] systems, the π* orbital of the bridge is populated and the stretching band appears at lower energies. In complex $\mathbf{3}^{4+}$, the ν(CN) band is also shifted to lower energies and a significant widening of the band is observed. The same happens for compound $\mathbf{4}^{4+}$ but in addition, the ν(CN) stretching loses intensity. This is due to a smaller change in the dipole moment that results from the more even distribution of the charge.[21] This behavior is also a consequence of the electronic delocalization in $\mathbf{3}^{4+}$ and $\mathbf{4}^{4+}$.

(TD)DFT calculations help us to assign the spectroscopy of the four mixed valence complexes. In agreement with the scenario presented in Figure 8, the five transitions with lower energy have the LUMOβ orbital as the acceptor. For $\mathbf{1}^{3+}$ this orbital is almost fully localized on $Ru_{b2}$ $d_{yz}$ orbital (6%$Ru_{tb}$, 67%$Ru_{b2}$), with *z* the axis connecting the two Ru atoms and *y* the axis containing the Ru-L bond. This orbital is the highest in energy among the dπ orbitals, due to its interaction with the L donor ligand. According to (TD)DFT calculations, the single broad band observed at 10750 $cm^{-1}$ is a convolution of the expected three IVCT transitions at 10797, 9328 and 8245 $cm^{-1}$ (Figure S4). The donor orbitals for the three transitions are mainly located on the $Ru_{tb}$ ion (Table S5 and Figure S13) and hence these transitions can be described as IVCT (Figure S14). In spite of that, there is significant mixing between the orbitals of both metal centers and a weak dependence on the nature of the solvent is expected

View Article Online
DOI: 10.1039/C7DT02422C



(Figure S4). The behavior of $\mathbf{2}^{3+}$ (Table S6 and Figures S15 and S16) is very similar to the described above for $\mathbf{1}^{3+}$. The band at 9500 $cm^{-1}$ is assigned to the convolution of three closed transition at 10285, 8381 and 7437 $cm^{-1}$ that have a similar origin to those described for complex $\mathbf{1}^{3+}$.

For $\mathbf{3}^{4+}$, the description begins to differentiate from the previous cases. Experimentally, the IVCT band is centered at 8400 $cm^{-1}$, but also two weaker bands at 3800 and 2200 $cm^{-1}$ can be resolved (Figure S8) that were not observed in the previous complexes. In this case, the acceptor orbital for the five transitions (LUMOβ) is more evenly distributed between both ruthenium centers (13% $Ru_{tb}$, 58% $Ru_{b2}$, Figure S16) than in the two previous cases. (TD)DFT calculations assign the first experimental band as three close transitions and also predict two more transitions on the red side of the spectrum. These transitions have more charge transfer character (Figure S18) and become more intense. This is in agreement with the experimental observation of these bands and links the observation of the two bands in the IR region to the more extensive mixing between the dπ orbitals of the Ru ions.

The experimental NIR absorption spectrum of compound $\mathbf{4}^{4+}$ shows three clearly resolved bands with maxima in 6900, 4200 and 1600 $cm^{-1}$ (Figure 9). Their assignment according to (TD)DFT calculations follows a similar pattern to the previous complexes. The five lowest-energy transitions have the LUMOβ as the orbital acceptor (Table S8, Figure S19), which in this system is more delocalized (27% $Ru_{tb}$, 48% $Ru_{b2}$). The most intense IVCT band is calculated at 6839 $cm^{-1}$, almost in perfect agreement with experimental value of 6900 $cm^{-1}$. For this band, the donor is mainly the HOMOβ, which is also very delocalized (48% $Ru_{tb}$, 26% $Ru_{b2}$). Transitions at 8080 and 1703 $cm^{-1}$ also start from delocalized orbitals (Table S9), but their orientation in space is different to that of the acceptor orbital, and for this reason, these are less intense than the one

View Article Online
DOI: 10.1039/C7DT02422C



discussed above. The other two transitions at 4213 and 5028 $cm^{-1}$ have their origin in $d_{xy}$ donor orbitals localized in each Ru center. It is worth value to note that these transitions are not properly described as IVCT or IC transitions as the acceptor orbital (LUMOβ) is not localized at one Ru center. In Figure 9, we fitted the NIR absorption features with five Gaussians centered at the energy value of the predicted transitions. These results show the usefulness of the (TD)DFT calculations at the performed level. They allow to understand the spectroscopy of these complexes, despite their intrinsic limitations which include the tendency to favor electronic delocalization and the lack of implementation of spin-orbit coupling effects.

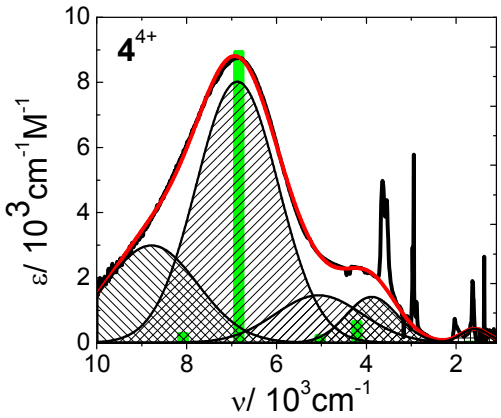


**Figure 9.** Gaussian deconvolution of the NIR absorption spectra of $\mathbf{4}^{4+}$

The observed evolution of the visible NIR spectra in this family of complexes can be used to analyze other Ru cyanide-bridged mixed-valence complexes in the literature. On one hand, complexes where the energy of the IVCT is higher than 9000 $cm^{-1}$ (like the complexes $\mathbf{1}^{3+}$ y $\mathbf{2}^{3+}$ reported here and many in literature[71–75,92]) are localized because the coordination sphere on one Ru center highly favors LUMO localization. These complexes present only one IVCT, and the CN stretch band is displaced to lower energies with an enhanced intensity. Despite the coordination spheres induce charge localization on one center, the cyanide bridge still promotes some degree of mixing of the dπ orbitals. These are Class II systems that can be described as

View Article Online
DOI: 10.1039/C7DT02422C



localized, where the localization is induced by the different coordination spheres around the Ru ions, and not by a weak coupling.

On the other hand, complexes where the IVCT is lower than 9000 $cm^{-1}$ (like complexes $\mathbf{3}^{4+}$ and $\mathbf{4}^{4+}$ reported here) present multiple low-energy bands that extend to the IR.[20,21] This indicates a more extensive mixing between the dπ orbitals of the Ru ions. In this kind of complexes, the most intense IVCT corresponds to a HOMOβ → LUMOβ transition that is often more intense and narrower than the IVCT transitions in other systems.[20] These compounds present an uneven charge distribution due to the non-symmetric nature of the coordination spheres, but cannot be described as localized systems either. For these systems, (TD)DFT calculations reproduce very well the energy of the most intense IVCT.[20] It is interesting to note the similitude between the properties of complex $\mathbf{4}^{4+}$ and those of $[Ru(tpy)(bpy)(\mu\text{-}NC)Ru(py)_4CN]^{3+}$ and $[Ru(tpm)(bpy)(\mu\text{-}NC)Ru(py)_4CN]^{3+}$.[20] The overall charge, the coordination spheres and the redox potentials of the fragments are very different; even more if compared with ruthenium dimers reported by Zhong et al.[93] However, the energy of the most intense band is similar and below 7000 $cm^{-1}$, indicating that the energies of the Ru fragments are close in the three cases. This is the key factor that triggers the extensive mixing of the dπ orbitals and the charge delocalization.

## Conclusions

The substitution of the L ligand in the bimetallic complexes presented here allowed us to fine tune the electronic communication between the ruthenium ions. This resulted in mixed-valence species with different degrees of mixing between the metallic dπ orbitals, ranging from a localized Class II system ($\mathbf{1}^{3+}$) to a delocalized Class III non-symmetrical mixed valence complex ($\mathbf{4}^{4+}$) with an uneven charge distribution. Additionally, we have been able to identify the spectroscopic signs that label the

View Article Online
DOI: 10.1039/C7DT02422C



process. These results illustrate the utility of the low energy transitions as a diagnostic tool for systems with substantial electronic mixing and the usefulness of DFT calculations to assign the spectroscopy and the charge distribution.

Our results show that the degree of delocalization can be controlled by the coordination spheres of the metallic ions. These variations in the electronic configuration of the bimetallic fragments could result in a very different reactivity. Hence, this possibility should be considered when exploring the ground- and excited-state catalytic properties of multimetallic systems, the latter of which appear to be less explored. The complexes reported here are being studied in this direction in our labs.

## Acknowledgments

This work was partially supported by the University of Buenos Aires (UBACyT q643 and q534), CONICET (PIP 0659) and ANPCyT (PICT 2013 0029 and PICT 2012 2041). The authors gratefully thank Prof. Dr. Pablo Alborés for XRD measurements and crystal structure refinement. LBV is member of the scientific staff of CONICET, and GEP, AC and PO acknowledge fellowship support from the same institution. GEP thanks Prof. Dr. Adrián Roitberg for selflessly sharing his knowledge and DAAD for personal funding. AC acknowledges a postdoctoral grant from DAAD and Ministerio de Educación, Ciencia y Tecnología (Argentina) and discussions within the ALN network about technical issues.

## References

1 M. K. Brennaman, R. J. Dillon, L. Alibabaei, M. K. Gish, C. J. Dares, D. L. Ashford, R. L. House, G. J. Meyer, J. M. Papanikolas and T. J. Meyer, *J. Am. Chem. Soc.*, 2016, **138**, 13085–13102.

View Article Online
DOI: 10.1039/C7DT02422C



2 D. L. Ashford, M. K. Gish, A. K. Vannucci, M. K. Brennaman, J. L. Templeton, J. M. Papanikolas and T. J. Meyer, *Chem. Rev.*, 2015, **115**, 13006–13049.
3 M. Grätzel, *Inorg. Chem.*, 2005, **44**, 6841–6851.
4 P. Day, N. S. Hush and R. J. H. Clark, *Philos. Trans. R. Soc. A Math. Phys. Eng. Sci.*, 2008, **366**, 5–14.
5 D. M. D'Alessandro and F. R. Keene, *Chem. Soc. Rev.*, 2006, **35**, 424–440.
6 K. D. Demadis, C. M. Hartshorn and T. J. Meyer, *Chem. Rev.*, 2001, **101**, 2655–2686.
7 J. J. Concepcion, D. M. Dattelbaum, T. J. Meyer and R. C. Rocha, *Philos. Trans. R. Soc. A Math. Phys. Eng. Sci.*, 2008, **366**, 163–175.
8 C. P. Kubiak, *Inorg. Chem.*, 2013, **52**, 5663–5676.
9 M. B. Robin and P. Day, in *Advances in Inorganic Chemistry and Radiochemistry*, 1968, vol. 10, pp. 247–422.
10 W.-W. Yang, J.-Y. Shao and Y.-W. Zhong, *Eur. J. Inorg. Chem.*, 2015, **2015**, 3195–3204.
11 J.-Y. Shao and Y.-W. Zhong, *Chem. - A Eur. J.*, 2014, **20**, 8702–8713.
12 F. Scandola, R. Argazzi, C. A. Bignozzi, C. Chiorboli, M. T. Indelli and M. A. Rampi, *Coord. Chem. Rev.*, 1993, **125**, 283–292.
13 J. F. Endicott and Y.-J. Chen, *Coord. Chem. Rev.*, 2013, **257**, 1676–1698.
14 S. Wang, X.-H. Ding, Y.-H. Li and W. Huang, *Coord. Chem. Rev.*, 2012, **256**, 439–464.
15 Y.-H. Li, W.-R. He, X.-H. Ding, S. Wang, L.-F. Cui and W. Huang, *Coord. Chem. Rev.*, 2012, **256**, 2795–2815.
16 K. R. Dunbar and R. A. Heintz, in *Progress in Inorganic Chemistry*, John Wiley & Sons, Inc., 1997, vol. 45, pp. 283–391.
17 L. M. Baraldo, P. Forlano, A. R. Parise, L. D. Slep and J. A. Olabe, *Coord. Chem. Rev.*, 2001, **219–221**, 881–921.
18 D. M. D'Alessandro and F. R. Keene, *Chem. Rev.*, 2006, **106**, 2270–2298.
19 M. B. Rossi, K. A. Abboud, P. Alborés and L. M. Baraldo, *Eur. J. Inorg. Chem.*, 2010, **2010**, 5613–5616.
20 G. E. Pieslinger, B. M. Aramburu-Trošelj, A. Cadranel and L. M. Baraldo, *Inorg. Chem.*, 2014, **53**, 8221–8229.
21 G. E. Pieslinger, P. Alborés, L. D. Slep and L. M. Baraldo, *Angew. Chemie Int. Ed.*, 2014, **53**, 1293–1296.
22 X. Ma, C.-S. Lin, X.-Q. Zhu, S.-M. Hu, T.-L. Sheng and X.-T. Wu, *Angew. Chemie Int. Ed.*, 2017, **56**, 1605–1609.
23 A. Cadranel, J. E. Tate, P. S. Oviedo, S. Yamazaki, J. H. Hodak, L. M. Baraldo and V. D. Kleiman, *Phys. Chem. Chem. Phys.*, 2017, **19**, 2882–2893.
24 E. C. Johnson, B. P. Sullivan, D. J. Salmon, S. A. Adeyemi and T. J. Meyer, *Inorg. Chem.*, 1978, **17**, 2211–2215.
25 A. Cadranel, P. Alborés, S. Yamazaki, V. D. Kleiman and L. M. Baraldo, *Dalt. Trans.*, 2012, **41**, 5343.
26 I. Noviandri, K. N. Brown, D. S. Fleming, P. T. Gulyas, P. A. Lay, A. F. Masters and L. Phillips, *J. Phys. Chem. B*, 1999, **103**, 6713–6722.
27 W. Kaim and J. Fiedler, *Chem. Soc. Rev.*, 2009, **38**, 3373.
28 C. SCALE3 ABSPACK: Empirical absorption correction, 2006.
29 A. Altomare, M. C. Burla, M. Camalli, G. L. Cascarano, C. Giacovazzo, A. Guagliardi, A. G. G. Moliterni, G. Polidori and R. Spagna, *J. Appl. Crystallogr.*, 1999, **32**, 115–119.
30 G. M. Sheldrick, *Acta Crystallogr. Sect. A Found. Crystallogr.*, 2008, **64**, 112–

View Article Online
DOI: 10.1039/C7DT02422C



122.
31 L. J. Farrugia, *J. Appl. Crystallogr.*, 2012, **45**, 849–854.
32 A. L. Spek, *Acta Crystallogr. Sect. C Struct. Chem.*, 2015, **71**, 9–18.
33 Gaussian 09, Revision D.01, M. J. Frisch, G. W. Trucks, H. B. Schlegel, G. E. Scuseria, M. A. Robb, J. R. Cheeseman, G. Scalmani, V. Barone, B. Mennucci, G. A. Petersson, H. Nakatsuji, M. Caricato, X. Li, H. P. Hratchian, A. F. Izmaylov, J. Bloino, G. Zheng, J. L. Sonnenberg, M. Hada, M. Ehara, K. Toyota, R. Fukuda, J. Hasegawa, M. Ishida, T. Nakajima, Y. Honda, O. Kitao, H. Nakai, T. Vreven, J. J. A. Montgomery, J. E. Peralta, F. Ogliaro, M. Bearpark, J. J. Heyd, E. Brothers, K. N. Kudin, V. N. Staroverov, T. Keith, R. Kobayashi, J. Normand, K. Raghavachari, A. Rendell, J. C. Burant, S. S. Iyengar, J. Tomasi, M. Cossi, N. Rega, J. M. Millam, M. Klene, J. E. Knox, J. B. Cross, V. Bakken, C. Adamo, J. Jaramillo, R. Gomperts, R. E. Stratmann, O. Yazyev, A. J. Austin, R. Cammi, C. Pomelli, J. W. Ochterski, R. L. Martin, K. Morokuma, V. G. Zakrzewski, G. A. Voth, P. Salvador, J. J. Dannenberg, S. Dapprich, A. D. Daniels, O. Farkas, J. B. Foresman, J. V. Ortiz, J. Cioslowski and D. J. Fox, 2013.
34 A. Szabo and N. S. Ostlund, *Modern Quantum Chemistry: Introduction to Advanced Electronic Structure Theory*, New York, 1996.
35 G. Scalmani and M. J. Frisch, *J. Chem. Phys.*, 2010, **132**, 114110.
36 J. Tomasi, B. Mennucci and R. Cammi, *Chem. Rev.*, 2005, **105**, 2999–3094.
37 S. Miertuš, E. Scrocco and J. Tomasi, *Chem. Phys.*, 1981, **55**, 117–129.
38 H. B. Schlegel, *J. Comput. Chem.*, 1982, **3**, 214–218.
39 L. Petit, P. Maldivi and C. Adamo, *J. Chem. Theory Comput.*, 2005, **1**, 953–962.
40 R. E. Stratmann, G. E. Scuseria and M. J. Frisch, *J. Chem. Phys.*, 1998, **109**, 8218–8224.
41 N. M. O'Boyle, A. L. Tenderholt and K. M. Langner, *J. Comput. Chem.*, 2008, **29**, 839–845.
42 GaussView, Version 6, R. Dennington, T. Keith and J. Millam, Semichem Inc., Shawnee Mission, KS, 2009.
43 F. Di Salvo, A. Crespo, D. A. Estrin and F. Doctorovich, *Tetrahedron*, 2002, **58**, 4237–4244.
44 P. Alborés, L. D. Slep, T. Weyhermüller and L. M. Baraldo, *Inorg. Chem.*, 2004, **43**, 6762–6773.
45 C.-N. Tsai, M. M. Allard, R. L. Lord, D.-W. Luo, Y.-J. Chen, H. B. Schlegel and J. F. Endicott, *Inorg. Chem.*, 2011, **50**, 11965–11977.
46 A. B. P. Lever, in *Comprehensive Coordination Chemistry II*, ed. T. J. M. B. T.-C. C. C. II, Elsevier, Oxford, 2003, pp. 251–268.
47 A. B. P. Lever, *Inorg. Chem.*, 1990, **29**, 1271–1285.
48 H. Rensmo, S. Lunell and H. Siegbahn, *J. Photochem. Photobiol. A Chem.*, 1998, **114**, 117–124.
49 S. Hohloch, D. Schweinfurth, M. G. Sommer, F. Weisser, N. Deibel, F. Ehret and B. Sarkar, *Dalt. Trans.*, 2014, **43**, 4437–4450.
50 S. Kämper, A. Paretzki, J. Fiedler, S. Záliš and W. Kaim, *Inorg. Chem.*, 2012, **51**, 2097–2104.
51 F. Cecchet, A. M. Gioacchini, M. Marcaccio, F. Paolucci, S. Roffia, M. Alebbi and C. A. Bignozzi, *J. Phys. Chem. B*, 2002, **106**, 3926–3932.
52 G. Wolfbauer, A. M. Bond and D. R. MacFarlane, *Inorg. Chem.*, 1999, **38**, 3836–3846.
53 P. Chen and T. J. Meyer, *Chem. Rev.*, 1998, **98**, 1439–1478.

View Article Online
DOI: 10.1039/C7DT02422C



54 J. R. Reimers, Z.-L. Cai and N. S. Hush, *Chem. Phys.*, 2005, **319**, 39–51.
55 N. Hush, *Coord. Chem. Rev.*, 1998, **177**, 37–60.
56 S. Gupta and D. V. Matyushov, *J. Phys. Chem. A*, 2004, **108**, 2087–2096.
57 A. Cadranel, G. E. Pieslinger, P. Tongying, M. K. Kuno, L. M. Baraldo and J. H. Hodak, *Dalt. Trans.*, 2016, **45**, 5464–5475.
58 M. B. Rossi, P. Alborés and L. M. Baraldo, *Inorganica Chim. Acta*, 2011, **374**, 334–340.
59 M. B. Rossi, O. E. Piro, E. E. Castellano, P. Alborés and L. M. Baraldo, *Inorg. Chem.*, 2008, **47**, 2416–2427.
60 P. Alborés, L. D. Slep, L. S. Eberlin, Y. E. Corilo, M. N. Eberlin, G. Benítez, M. E. Vela, R. C. Salvarezza and L. M. Baraldo, *Inorg. Chem.*, 2009, **48**, 11226–11235.
61 J. Bendix, P. Steenberg and I. Søtofte, *Inorg. Chem.*, 2003, **42**, 4510–4512.
62 L. Toma, L. Toma, F. Delgado, C. Ruiz-Pérez, J. Sletten, J. Cano, J. Clemente-Juan, F. Lloret and M. Julve, *Coord. Chem. Rev.*, 2006, **250**, 2176–2193.
63 S. F. A. Kettle, G. L. Aschero, E. Diana, R. Rossetti and P. L. Stanghellini, *Inorg. Chem.*, 2006, **45**, 4928–4937.
64 S. F. A. Kettle, E. Diana, E. Boccaleri and P. L. Stanghellini, *Inorg. Chem.*, 2007, **46**, 2409–2416.
65 S. F. A. Kettle, E. Diana, E. M. C. Marchese, E. Boccaleri, G. Croce, T. Sheng and P. L. Stanghellini, *Eur. J. Inorg. Chem.*, 2010, **2010**, 3920–3929.
66 C. A. Bignozzi, R. Argazzi, J. R. Schoonover, K. C. Gordon, R. B. Dyer and F. Scandola, *Inorg. Chem.*, 1992, **31**, 5260–5267.
67 S. Alvarez, C. López and M. J. Bermejo, *Transit. Met. Chem.*, 1984, **9**, 123–126.
68 D. A. Dows, A. Haim and W. K. Wilmarth, *J. Inorg. Nucl. Chem.*, 1961, **21**, 33–37.
69 G. E. Pieslinger, P. Alborés, L. D. Slep, B. J. Coe, C. J. Timpson and L. M. Baraldo, *Inorg. Chem.*, 2013, **52**, 2906–2917.
70 S. Siddiqui, W. W. Henderson and R. E. Shepherd, *Inorg. Chem.*, 1987, **26**, 3101–3107.
71 C. A. Bignozzi, C. Paradisi, S. Roffia and F. Scandola, *Inorg. Chem.*, 1988, **27**, 408–414.
72 E. H. Cutin and N. E. Katz, *Polyhedron*, 1993, **12**, 955–960.
73 W. M. Laidlaw and R. G. Denning, *J. Chem. Soc. Dalt. Trans.*, 1994, 1987.
74 A. Ponce, M. Bachrach, P. J. Farmer and J. R. Winkler, *Inorganica Chim. Acta*, 1996, **243**, 135–140.
75 A. V. Macatangay and J. F. Endicott, *Inorg. Chem.*, 2000, **39**, 437–446.
76 F. Roncaroli, L. M. Baraldo, L. D. Slep and J. A. Olabe, *Inorg. Chem.*, 2002, **41**, 1930–1939.
77 T.-L. Sheng and H. Vahrenkamp, *Eur. J. Inorg. Chem.*, 2004, **2004**, 1198–1203.
78 V. Coropceanu, M. Malagoli, J. M. André and J. L. Brédas, *J. Am. Chem. Soc.*, 2002, **124**, 10519–10530.
79 A. J. Cohen, P. Mori-Sanchez and W. Yang, *Science (80-. ).*, 2008, **321**, 792–794.
80 M. Renz and M. Kaupp, *J. Phys. Chem. A*, 2012, **116**, 10629–10637.
81 A. J. Cohen, P. Mori-Sánchez and W. Yang, *Chem. Rev.*, 2012, **112**, 289–320.
82 J.-L. Lin, C.-N. Tsai, S.-Y. Huang, J. F. Endicott, Y.-J. Chen and H.-Y. Chen, *Inorg. Chem.*, 2011, **50**, 8274–8280.
83 B. S. Brunschwig, C. Creutz and N. Sutin, *Chem. Soc. Rev.*, 2002, **31**, 168–184.
84 K. D. Demadis, G. A. Neyhart, E. M. Kober, P. S. White and T. J. Meyer, *Inorg.*

View Article Online
DOI: 10.1039/C7DT02422C

*Chem.*, 1999, **38**, 5948–5959.
85 K. D. Demadis, E.-S. El-Samanody, G. M. Coia and T. J. Meyer, *J. Am. Chem. Soc.*, 1999, **121**, 535–544.
86 W. Kaim and B. Sarkar, *Coord. Chem. Rev.*, 2013, **257**, 1650–1659.
87 D. M. D'Alessandro, P. H. Dinolfo, M. S. Davies, J. T. Hupp and F. R. Keene, *Inorg. Chem.*, 2006, **45**, 3261–3274.
88 R. C. Rocha, F. N. Rein, H. Jude, A. P. Shreve, J. J. Concepcion and T. J. Meyer, *Angew. Chemie Int. Ed.*, 2008, **47**, 503–506.
89 C.-J. Yao, Y.-W. Zhong and J. Yao, *J. Am. Chem. Soc.*, 2011, **133**, 15697–15706.
90 J. F. Endicott, P. G. McNamara, T. Buranda and A. V Macatangay, *Coord. Chem. Rev.*, 2000, **208**, 61–75.
91 M. A. Watzky, J. F. Endicott, X. Song, Y. Lei and A. Macatangay, *Inorg. Chem.*, 1996, **35**, 3463–3473.
92 F. W. Vance, R. V. Slone, C. L. Stern and J. T. Hupp, *Chem. Phys.*, 2000, **253**, 313–322.
93 J.-H. Tang, J.-Y. Shao, Y.-Q. He, S.-H. Wu, J. Yao and Y.-W. Zhong, *Chem. - A Eur. J.*, 2016, **22**, 10341–10345.

View Article Online
DOI: 10.1039/C7DT02422C

**For Table of Contents Only**

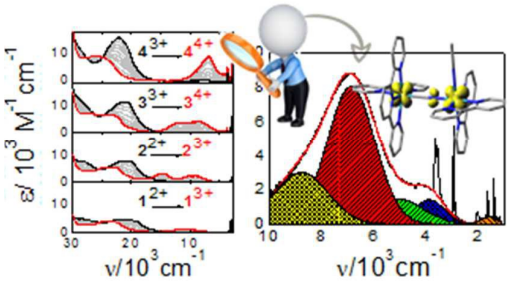


*"Modification of the ligand L in the mixed-valence cyanide-bridged complexes [Ru(tpy)(bpy)(μ-CN)Ru(bpy)$_2$(L)]$^{3+/4+}$ (L= Cl$^-$ (**1**$^{2+}$), NCS$^-$ (**2**$^{2+}$), 4-dimethylaminopyridine (**3**$^{3+}$) or acetonitrile (**4**$^{3+}$)) reduces the difference between the redox potentials of the ruthenium ions. This change brings a modification on the properties of the observed intervalence charge transfer bands that can be understood as a transition from a localized to a delocalized configuration on the basis of DFT calculations. (TD)DFT calculations allow us to assign in detail these transitions, including the four experimentally resolved bands for the acetonitrile complex"*